*Mineralogical Magazine, April 2015, Vol. 79(2), pp. 437–458*

OPEN ACCESS

# Alteration of nanocrystalline calcium silicate hydrate (C-S-H) at pH 9.2 and room temperature: a combined mineralogical and chemical study

NICOLAS C. M. MARTY[1,*], SYLVAIN GRANGEON[1], FABIENNE WARMONT[2] AND CATHERINE LEROUGE[1]

[1] BRGM, D3E/SVP, 3 Avenue C. Guillemin, F-45060 Orléans Cedex 2, France
[2] ICMN (Interface, Confinement, Matériaux et Nanostructures) – UMR 7374 – CNRS – Université d'Orléans, 1b rue de la Férollerie, 45071 Orléans Cedex 2, France

[*Received 26 May 2014; Accepted 4 September 2014; Associate Editor: G. D. Gatta*]

## ABSTRACT

Calcium silicate hydrate (C-S-H) alteration was studied with flow-through experiments at 25ºC and pH 9.2. Three materials with apparent Ca/Si ratios (C/S ratios) of 1.47, 1.38 and 0.86 were investigated. Physical (thermogravimetric analyses/differential thermal analysis), mineralogical (X-ray diffraction) and chemical (electron probe microanalysis, transmission electron microscopy/energy dispersive X-ray spectrometry) analyses were performed to characterize the reacting minerals. Initial stoichiometric C/S ratios were 1.22, 1.22 and 0.85, respectively. The excess of Ca is attributed mainly to the presence of calcium hydroxide intimately mixed in with C-S-H particles.

The C-S-H chemical compositions were monitored during flow-through experiments in order to determine the mineral stoichiometry needed for reaction kinetics. Under our experimental conditions the stoichiometric C/S ratios decreased continuously with time. A close to stoichiometric dissolution was observed after 2 days of experiments. Using an integrated approach, the kinetics was found to be a function of the C/S.

A decrease in layer-to-layer distance in the early stage of the alteration process is interpreted as interlayer Ca/Na exchange (Na being part of the pH buffering solution). A second dissolution step, marked by a close to stoichiometric release of Ca and Si, undoubtedly results from layer dissolution. The structural similarity of C-S-H and tobermorite was confirmed.

**KEYWORDS:** calcium silicate hydrate, C-S-H, dissolution, kinetics, alteration product.

## Introduction

NANOCRYSTALLINE calcium silicate hydrates (C-S-H) are the main constituents of Portland and 'low-pH' concretes (e.g. Bach *et al.*, 2012; Brunauer, 1962; McCulloch *et al.*, 1985; Richardson, 2008) and control the main chemical (e.g. Blanc *et al.*, 2010; Glasser, 2001) and physical (Manzano *et al.*, 2007) properties of cement. It is therefore fundamentally important that we are able to reliably estimate C-S-H weathering/dissolution rates if we wish to estimate the durability of various cementitious materials (e.g. Baston *et al.*, 2012; Savage, 2011; Trapote-Barreira *et al.*, 2014). Such estimations are undertaken efficiently using kinetic laws, which are used to predict the behaviour of radioactive waste repositories (e.g. Hoch *et al.*, 2012; Marty *et al.*, 2009; Watson *et al.*, 2012) or of wellbore cement in $CO_2$ confinement sites (e.g. Gherardi *et al.*, 2012; Wilson *et al.*, 2011).

Calcium silicate hydrates are characterized by their chemical variability in terms of the Ca to Si ratio (i.e. their C/S ratio), which is usually reported to range between ~0.6 and ~2.3 with very fine-scale heterogeneity when they are formed from hydration of cement components (Richardson, 2004, 2008),

* E-mail: n.marty@brgm.fr
DOI: 10.1180/minmag.2015.079.2.20

and thus by the variability of their crystal structure. It is generally accepted that C-S-H, at least at low C/S ratios (<~1.25), have a structure that is close to tobermorite [$Ca_4Si_6O_{15}(OH)_2{\cdot}5H_2O$ according to Merlino *et al.* (1999), although the actual stoichiometry is variable], and are nanometre sized (Skinner *et al.*, 2010). Modelling of X-ray diffraction (XRD) patterns from C-S-H samples with a C/S ratio of 0.82 to 0.87 also argues for a tobermorite-like structure affected by nanocrystallinity and turbostratic disorder (Grangeon *et al.*, 2013*a*,*b*). Turbostratism would explain the observed transformation of C-S-H to tobermorite upon heating (Houston *et al.*, 2009) by a simple improvement of layer stacking.

In contrast, the description of the structure of C-S-H with a high C/S ratio (>~1.25) is still subject to debate: some authors assume that the crystal structure is close to that of jennite ($Ca_9Si_6O_{18}(OH)_6{\cdot}8H_2O$ – Bonaccorsi *et al.*, 2004), whereas others describe the structure as an intimate mixing, at the nanoscale (Chen *et al.*, 2010; Vandamme and Ulm, 2013), of tobermorite with calcium hydroxide (e.g. Cong and Kirkpatrick, 1996; Nonat, 2004; Richardson, 2004, 2008; Taylor, 1986).

Several studies have shown that the C/S ratio decreases as alteration progresses; incongruent leaching of C-S-H gives decreasing pH from 12.5 to 10.5 (Butcher *et al.*, 2012; Harris *et al.*, 2002; Trapote-Barreira *et al.*, 2014; Vieillard and Rassineux, 1992) whereas a congruent dissolution is observed with a C/S of ~0.85 at pH = 10.5 (Baston *et al.*, 2012; Harris *et al.*, 2002; Trapote-Barreira *et al.*, 2014; Vieillard and Rassineux, 1992). Assuming that the tobermorite structure is a valid analogy of C-S-H with a low C/S ratio, the C-S-H structure should be unstable for C/S ratios below ~0.66, as this ratio corresponds to that of a tobermorite having infinite silicate chains and no interlayer Ca (Merlino *et al.*, 2001). From previous studies (Baston *et al.*, 2012; Blanc *et al.*, 2010; Harris *et al.*, 2002), C-S-H of such a ratio should be unstable at pH <~10.

Understanding, and thus being able to predict and model, the dissolution of C-S-H requires a sound understanding of the relation between the crystal structure from these materials and the kinetics of dissolution. To our knowledge, only Trapote-Barreira *et al.* (2014) and Baston *et al.* (2012) have studied the alteration of C-S-H by investigating both solution chemistry and the mineralogical evolution, but only the former provided a detailed discussion of chemical and mineralogical evolution during the experiments. In particular, the crystallographic evolution was monitored. However, they only focused on samples having a C/S ratio of 1.7 ± 0.1 and containing significant portlandite (~30 wt.%). They observed an incongruent dissolution when the C/S ratio is high and then a congruent dissolution as the C/S ratio decreases to the tobermorite stoichiometric C/S ratio of 0.83. A similar evolution has been already observed by Harris *et al.* (2002) and Baston *et al.* (2012). However, although the study by Trapote-Barreira *et al.* (2014) provides valuable data, their flow-through experiments were performed at pH ranging from 12.5 to 10 using material containing portlandite, and with C-S-H of high initial C/S ratio (i.e. C/S of 1.7). Therefore additional studies on C-S-H of lower ratio, which are typical for low-pH cements, and of materials as pure as possible are necessary to increase our understanding of C-S-H chemical reactivity and provide relevant kinetic parameters. Investigating dissolution occurring at lower pH values is also mandatory to understand better the dissolution that can occur in various environments, for example at a clay/cement interface where high pH conditions are attenuated (e.g. Baston *et al.*, 2012; Marty *et al.* 2009, 2011).

The objectives of the present study, which combines dissolution experiments with physical characterization methods (thermogravimetric measurements, powder XRD, transmission electron microscopy) were twofold. First, the kinetics law for the dissolution of C-S-H with a bulk C/S ratio varying between 1.47 and 0.86 was retrieved. Secondly, the evolution of the C-S-H structure during dissolution was monitored in order to understand better the structural mechanisms of C-S-H dissolution. To this end, the initial material was first examined carefully using a combination of chemical and physical techniques. Dissolution experiments were then undertaken in flow-through reactors at slightly basic pH (~9) and room temperature (~25ºC). Alteration products were examined carefully at completion of the experiments.

## Materials and methods

### *Materials*

#### *C-S-H samples*

Samples from the present study are labelled C-S-H_X.Xi (initial products) and C-S-H_X.Xf (final products), where X.X stands for the bulk atomic C/S ratio which, as discussed hereafter, is



https://doi.org/10.1180/minmag.2015.079.2.20 Published online by Cambridge University Press

equal to 0.9, 1.4 and 1.5. They were synthesized by Hokkaido University at 170, 80 and 50ºC for CSH_1.5i, CSH_0.9i and CSH_1.4i, respectively. The procedure is described in Grangeon *et al.* (2013*b*). During their transport to the BRGM laboratory, samples were kept encapsulated to avoid contact with the atmosphere. They were then were stored in a glove-box (Jacomex GP, $pO_2$ <3 ppm). For calculations, the C-S-H stoichiometry was normalized with one mole of silica as $(CaO)_{C/S}SiO_2{\cdot}xH_2O$.

#### *Input solutions*

All solutions were prepared with ultra-pure water (Milli-Q; resistivity >18 MΩ) and continuously bubbled with $N_2$. The objective was to suppress the $CO_2$ partial pressure in order to avoid C-S-H carbonation (Suzuki *et al.*, 1985) during flow-through experiments. The input solution was made up of borax (0.01 M $Na_2B_4O_7{\cdot}10H_2O$) with a buffer pH of ~9.2 at 25ºC.

### *Analytical procedures*

#### *Solid analysis*

An electron probe microanalyser (EPMA) was used to determine the chemical compositions before and after dissolution experiments. Analyses of C-S-H were carried out on polished thin sections using a Cameca SX Five electron microprobe with an acceleration voltage of 15 kV, a beam current of 12 nA and a 1–2 μm beam width. Peak and background counting times were 10 s. Prior to analysis, a 10–20 nm thick carbon layer was sputter-coated on the samples (Edwards Auto 306). The system was calibrated with a variety of synthetic oxides and pure elements: albite [$NaAlSi_3O_8$] for Na and Si, synthetic $Al_2O_3$ for Al, synthetic $Fe_2O_3$ for Fe, synthetic MgO for Mg, orthoclase [$KAlSi_3O_8$] for K and wollastonite [$CaSiO_3$] for Ca. Ca*K*α and K*K*α were monitored using a PET (pentaerythritol) crystal, Fe*K*α using a LiF (lithium fluoride) crystal, and Al*K*α, Mg*K*α, Na*K*α and Si*K*α using a TAP (thallium acid phthalate) crystal. Matrix corrections were carried out with a *ZAF* program (Merlet, 1994).

Characterization and identification of all samples but CSH_1.5f at the end of the experiment were undertaken by XRD using a Bruker D5000 diffractometer equipped with a Co anode ($\lambda\ K\alpha_1$ = 1.78897 Å). Samples were rotated during analysis, which was performed in step-scan mode, with intensities recorded in the 4–84º2θ range with an 11 s counting time per 0.04º2θ step for initial samples and a 6 s counting time for final samples, in which a rutile standard was inserted to ensure the robustness of measured angular positions. Sample CSH_1.5f was analysed using different analytical conditions because of the very small amount of sample remaining after the experiment (<5 mg). The XRD pattern was acquired in the 4–84º2θ angular range using a Bruker D8 Advance diffractometer, using Co*K*α radiation, on a rotated Si monocrystal sample holder, with diffracted intensity recorded in continuous mode using a LynxEye 1D detector (angular width = 3.3º) and 24 h of recording time.

C-S-H samples were analysed prior to, during, and after dissolution experiments using transmission electron microscopy (TEM) and energy dispersive X-ray spectrometry (EDX). For the initial and final stages, TEM samples were prepared by dispersing the powdered samples in alcohol by ultrasonic treatment. One drop of the suspension was deposited on the carbon membrane and the solvent was evaporated at room temperature. High-resolution TEM images were taken using a CM20 PHILIPS operating at 200 kV with a line resolution of 1.4 Å.

Thermogravimetric analyses (TGA) and differential scanning calorimetry (DSC) were performed simultaneously using a high-performance thermogravimetric analyser (SETSYS Evolution). A heating rate of 10ºC $min^{-1}$ until 1600ºC under flowing nitrogen was imposed. Only initial C-S-H samples were analysed. Prior to analysis, the materials had been stored for 10 days at 11% relative humidity using $LiCl_2$ salts under $N_2$ atmosphere.

#### *Solution analysis*

The pH was measured immediately after sampling. The apparatus (a Metrohm electrode connected to a Mettler Toledo pH meter) was calibrated before each analysis. Collected fluids were then acidified using nitric acid (65% Suprapur®). Calcium and silicon concentrations were measured by inductively coupled plasma atomic emission spectroscopy (ICP-AES, Jobin Yvon Horiba Ultima sequential spectrometer). The detection limits were 0.5 mg $l^{-1}$ for both Ca and $SiO_2$.

### *Flow-through experiments*

#### *Experimental apparatus*

Experiments were carried out on three different samples (CSH_1.5i, CSH_1.4i and CSH_0.9i)



https://doi.org/10.1180/minmag.2015.079.2.20 Published online by Cambridge University Press

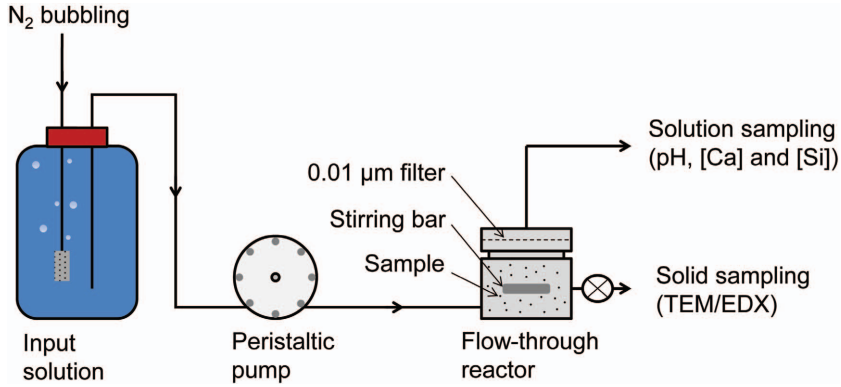


FIG. 1. The experimental apparatus.

using flow-through reactors at room temperature (Fig. 1). The total volume of the reactor was ~83 ml. The input buffer solution was circulated at a constant flow rate between 0.49 and 0.58 ml $min^{-1}$ through the reactors using a peristaltic pump (Watson Marlow, 205U). The input solution was bubbled continuously with $N_2$. The magnetic stirrer was rotated on an axle in order to avoid any grinding of C-S-H particles between the bar and the bottom of the reactor (Metz and Ganor, 2001). Initial mass and the average flow rates are given in Table 1.

### *Solution sampling*

The output solution was filtered through a 0.01 µm membrane before being collected in the output bottle (Cellulose nitrate filter, Sartorius). The sampling allows the monitoring of solution chemistry (pH, Ca and Si concentrations) as well as flow rates as a function of time.

### *Solid sampling*

A tap above the filter enabled the collection of the solid during experiments. Only one drop of C-S-H suspension on a grid is needed for TEM/EDX analysis. Therefore the effects of procedure on the total amount of C-S-H can be ignored. The solid suspension was also collected and filtered (using filters of 0.01 µm cut-off diameter) at the end of the experiment. This provided enough solid so that characterization could also be undertaken with other methods (TEM/EDX, EPMA and XRD). The masses of recovered materials at the end of the experiments are reported in Table 1. The loss of material appears to be unavoidable during the procedure. Uncertainties on final-mass measurements are therefore very large (probably >15%). However the masses collected and calculated from solution chemistries are in the same order of magnitude (see the Appendix which has been deposited with the Principal Editor of *Mineralogical Magazine* and is available from www.minersoc.org/pages/e_journals/dep_mat_mm.html).

## Calculation methods

### *Dissolution rates*

The stirred flow-through reactors enable good control of the reaction conditions (i.e. constant pH

TABLE 1. Experimental conditions.

| Experiment | Average flow rate (ml $min^{-1}$) | Initial mass (g) | Final mass (g) |
|---|---|---|---|
| CSH_1.5 | 0.486 | 1.1934 | < 0.005 |
| CSH_1.4 | 0.578 | 1.1876 | 0.1093 |
| CSH_0.9 | 0.566 | 1.1751 | 0.5293 |



https://doi.org/10.1180/minmag.2015.079.2.20 Published online by Cambridge University Press

conditions using a buffer solution as input). The experimental setup is very effective for the measurement of reaction rates at a steady state (reached when the outlet concentrations are constant with time). In the case of a congruent reaction, the following expression is valid (Lasaga, 1998):

$$\frac{dN_i}{dt} = 0 = -V(c_{out} - c_{in}) + \varepsilon_i A_n k_n \qquad (1)$$

where $N_i$ is the amount of species i (mol), $t$ is the time (s), $v$ is the flow rate (l $s^{-1}$), $c_{out}-c_{in}$ is the difference between inlet and outlet concentrations (mol $l^{-1}$), ε is the stoichiometry of the species inside the mineral n, $A$ is the reactive surface of the mineral ($m^2$) and k is the kinetic constant (mol $m^{-2}$ $s^{-1}$).

Therefore:

$$k_n = \frac{v(c_{out} - c_{in})}{\varepsilon_i A_n} \qquad (2)$$

As indicated in equation 2, the rate constant is estimated according to the stoichiometric coefficient (ε = C/S for Ca and ε = 1 for Si) and the reactive surface area ($A$). However, these parameters change during our dissolution experiments. It is therefore essential to know the C/S ratio (i.e. ε) and the reactive surface area during the dissolution experiment in order to determine the rate constants.

### C/S ratios obtained from direct measurements

Initial and final C/S ratios were determined from TEM/EDX and EPMA analysis. The atomic ratio was also measured directly by TEM/EDX analysis during the flow-through experiment. The average ratio was calculated from EDX measurement of ~15 particles. Unfortunately, this technique is subject to uncertainties due to the limited amount of C-S-H analysed. However, as opposed to EPMA, EDX allows positively identified C-S-H particles to be selected (i.e. material free from impurities). The method is therefore efficient for monitoring the solid composition as function of time.

### C/S ratios estimated from indirect measurements

The TGA/DSC experiments were conducted to estimate the initial abundance of impurities such as calcium hydroxide (CH) and calcium carbonate ($CaCO_3$), following previous studies (Kim *et al.*, 2013; Morandeau *et al.*, 2014). From comparison between these derived amounts of impurities and the bulk C/S ratio, the initial stoichiometry for the synthetic C-S-H samples was determined.

The derived thermogravimetric curve (DTG) and DSC have been used to determine the temperature ranges corresponding to loss of water from CH and loss of $CO_2$ from $CaCO_3$ aggregates (Villain *et al.*, 2007). The loss of water from C-S-H occurs between 90 and 350ºC. Water is removed from CH within a temperature range of 350−600ºC. The loss of mass within a temperature range of 700−850ºC reflects the loss of $CO_2$ from $CaCO_3$. Mass percentages of $Ca(OH)_2$ ($m_{CH}$ in %) and $CaCO_3$ ($m_{CaCO_3}$ in %) are obtained from equations 3 and 4:

$$m_{CH} = \frac{m_{CH}^{water} M_{CaO}}{M_{H_2O}} + m_{CH}^{water} \qquad (3)$$

$$m_{CaCO_3} = \frac{m_{CaCO_3}^{CO_2} M_{CaO}}{M_{CO_2}} + m_{CaCO_3}^{CO_2} \qquad (4)$$

where $m_{CH}^{water}$ is the loss of mass (%) when water is removed from $Ca(OH)_2$ and $m_{CaCO_3}^{CO_2}$ is the loss of mass (%) when $CO_2$ is removed from $CaCO_3$ aggregates. $M_{H_2O}$, $M_{CO_2}$ and $M_{CaO}$ are the molar mass (g $mol^{-1}$) of $H_2O$, $CO_2$ and CaO, respectively.

After the CH and $CaCO_3$ contents have been determined, the residual mass is considered to be C-S-H ($m_{CSH}$ in %):

$$m_{CSH} = 100 - \left(\frac{m_{CH}^{water} M_{CaO}}{M_{H_2O}} + m_{CH}^{water}\right) - \left(\frac{m_{CaCO_3}^{CO_2} M_{CaO}}{M_{CO_2}} + m_{CaCO_3}^{CO_2}\right) \qquad (5)$$

The actual C/S ratio of C-S-H (i.e. free of any associated impurity) verifies:

$$C/S_{bulk} = \frac{C/S\frac{m_{CSH}}{M_{CSH}} + \frac{m_{CH}}{M_{CH}} + \frac{m_{CaCO_3}}{M_{CaCO_3}}}{\frac{m_{CSH}}{M_{CSH}}} \qquad (6)$$

where $M_{CH}$, $M_{CaCO_3}$ and $M_{CSH}$ are the molar mass (g $mol^{-1}$) of $Ca(OH)_2$, $CaCO_3$ and C-S-H, respectively (n.b. C-S-H stoichiometry normalized with one mole of silica). The Ca/Si ratio of the bulk, $C/S_{bulk}$, is measured directly using EPMA.



https://doi.org/10.1180/minmag.2015.079.2.20 Published online by Cambridge University Press

### *C/S ratios estimated from solution analysis*

The C/S ratio can be estimated as function of time from the evolution of the solution composition. This is expressed by:

$$C/S_t = \frac{Ca_i - \sum_t Ca_t}{Si_i - \sum_t Si_t} \quad (7)$$

where subscript t denotes (and in all following equations) a value obtained at a given time of the experiment.

The initial amounts of calcium and silicon ($Ca_i$ and $Si_i$ in mol) are estimated from the mass of C-S-H entering the flow-through reactor:

$$Ca_i = \frac{m_i}{M_{CSH_i}} C/S_i \quad (8)$$

$$Si_i = \frac{m_i}{M_{CSH_i}} \quad (9)$$

where $m_i$ is the initial mass of added C-S-H (g), $M_{CSH_i}$ is its initial molar mass (g mol$^{-1}$) and $C/S_i$ is the initial C/S ratio (determined by TGA experiments).

The cumulative evolution of Ca and Si are given by:

$$\sum_t Ca_t = \sum_t V_t \left( [Ca]_t^{out} - [Ca]_t^{in} \right) \quad (10)$$

$$\sum_t Si_t = \sum_t V_t \left( [Si]_t^{out} - [Si]_t^{in} \right) \quad (11)$$

where $V$ is the volume of sampled solution (l) and $[Ca]$ and $[Si]$ are the total Ca and Si concentrations (mol l$^{-1}$). All of the liquid flowing through the reactor was sampled and analysed.

The samples in the present study are not pure and include a non-negligible proportion of CH (Table 2). Assuming a rapid dissolution of Ca impurities (e.g. CH particles) in the early stages, the general expression (equation 7) of the C/S ratio was modified as follows:

$$C/S_t = \frac{Ca_i - \sum_t Ca_t}{Si_i - \sum_t Si_t} + \sigma \quad (12)$$

where $\sigma$ is the correction factor due to the presence of Ca impurities, estimated as the difference between the C/S ratio estimated for the bulk (EPMA) and pure particles (TGA).

### *Reactive surface area*

Kantro *et al.* (1962) showed that the specific surface area depends on the C/S ratio. The relationship was obtained from studies by Brunauer (1962), whose equation was calculated using the least-squares straight line, based on 44 pastes, as a function of the C/S ratio:

$$SSA_t = 865.0(\pm 42.9) - (354.7(\pm 39.9))C/S_t \quad (13)$$

where $SSA$ is the specific surface area (m$^2$ g$^{-1}$).

The reactive surface area ($A$) and the specific surface area ($SSA$) satisfy the relation:

$$A_t = SSA_t m_t \quad (14)$$

where $A$ is the reactive surface area (m$^2$) and $m$ is the mass of C-S-H inside the flow-through reactor (g).

TABLE 2. Initial characterization of C-S-H samples.

| Sample | Average C/S from EPMA | Average C/S from TEM/EDX | C/S from TGA/DSC | Difference EPMA/TGA ($\sigma$) | Accessory minerals | Mass percent of impurities (%) |
|---|---|---|---|---|---|---|
| CSH_1.5i | 1.47 ± 0.04 ($n$ = 59) | 1.22 ± 0.24 ($n$ = 19) | 1.22 | 0.25 | CH<br>Calcite | 9.31<br>0.68 |
| CSH_1.4i | 1.38 ± 0.03 ($n$ = 60) | 1.21 ± 0.12 ($n$ = 18) | 1.22 | 0.16 | CH<br>Calcite | 6.45<br>0.42 |
| CSH_0.9i | 0.86 ±0.01 ($n$ = 50) | 0.85 ± 0.06 ($n$ = 12) | 0.85 | 0.01 | CH<br>Calcite | –<br>0.49 |

$n$ = number of independent analyses.



https://doi.org/10.1180/minmag.2015.079.2.20 Published online by Cambridge University Press

### *Mass sample evolution*

As discussed hereafter, the results indicate a preferential release of Ca. Moreover, TEM/EDX and TGA/DSC analyses reveal the presence of Ca impurities (CH, $CaCO_3$). Therefore, the mass of C-S-H remaining in the reactor cannot be calculated from output Ca concentrations. The current mass is only updated according to the silicon concentration:

$$m_t = (1 - \alpha_i)m_i - \sum_t V_t\left([Si]_t^{out} - [Si]_t^{in}\right)M_{CSH_t} \quad (15)$$

where $\alpha_i$ is the mass fraction of impurities in the initial material (Table 2).

The structural formula of the C-S-H changes during the dissolution process (decrease in the C/S ratio). Therefore, the molar mass of the material is also updated. The molar masses of various C-S-H phases extracted from the *THERMODDEM* database (Blanc *et al.*, 2012) are given in Table 3. The evolution of the molar mass as a function of the C/S ratio is very well modelled with a linear regression (i.e. $r^2 \sim 1$):

$$M_{CSH_t} = 77.979C/S_t + 71.211 \quad (16)$$

## Characterization of the initial material

### *Physical and chemical characterizations*

The EPMA gave bulk C/S ratios of 1.47 (±0.04), 1.38 (±0.03) and 0.86 (±0.01) for CSH_1.5i, CSH_1.4i and CSH_0.9i, respectively (Table 2). Although the standard deviation is small, possible systematic analysis of accessory minerals cannot be ruled out owing to the fact that the beam size (~1−2 μm) is larger than the size of C-S-H particles (typically <50 nm; Skinner *et al.*, 2010).

The XRD patterns from C-S-H samples are shown in Fig. 2. At the sensitivity levels of this method, all C-S-H samples are free of crystallized phases, as all diffraction maxima are attributable to C-S-H. In particular, using the structure model from Grangeon *et al.* (2013*b*), the maxima located at ~7.6º2θ, 34.1º2θ, 37.3º2θ and 58.6º2θ are attributed respectively to the (001) basal reflection, and to the (02,$\bar{2}$2), (20) and ($\bar{2}$4) bands. The most obvious difference between the XRD patterns of the three samples is the position of the (001) reflection, which varies in position and intensity. It is located at ~7.6º2θ (~13.5 Å) in CSH_0.9i, ~8.6º2θ (~11.9 Å) in CSH_1.4i, and is almost absent in C-S-H_1.5i. The reduction in the layer-to-layer distance between CSH_0.9i and CSH_1.4i is in agreement with the literature data (Garbev *et al.*, 2008; Grangeon *et al.*, 2013*a*; Renaudin *et al.*, 2009). The absence of this reflection in CSH_1.5i may indicate that C-S-H crystals are built up of monolayers, or that layer parallelism is lost, as a result of structural strains (e.g. layer bending, observed frequently in nanocrystalline layered minerals, Hadi *et al.*, 2014; Manceau *et al.*, 2013) or of the inclusion of impurities in the interlayer space (Lanson *et al.*, 2008). Another variation between all XRD patterns is the region between the (02,$\bar{2}$2) and (20) bands: from CSH_0.9i to CSH_1.4i, a 'hump' on the high-angle side of the (02,$\bar{2}$2) band appears, and between CSH_1.4i and CSH_1.5i, the diffracted intensity between these two bands is much greater in the latter, which is compatible with a further intensity increase in the 'hump' on the high-angle side of the (02,$\bar{2}$2) band. This might be related to a structural evolution in the C-S-H structure and/or the presence of limited amounts of a calcite-like structure, of which the most intense diffraction maximum is at 34.3º2θ (3.035 Å).

The TEM examinations reveal a foil-like morphology. Well crystallized calcite is observed in CSH_1.5i (Fig. 3). The nature of these impurities is confirmed by both EDX analyses

TABLE 3. C-S-H properties extracted from the *THERMODDEM* database (Blanc *et al.*, 2012).

| C/S ratio | Structural formula | Molar mass (g $mol^{-1}$) |
|---|---|---|
| 1.6 | $Ca_{1.6}SiO_{3.6}{\cdot}2.58H_2O$ | 196.285 |
| 1.2 | $Ca_{1.2}SiO_{3.2}{\cdot}2.06H_2O$ | 164.486 |
| 0.8 | $Ca_{0.8}SiO_{2.8}{\cdot}1.54H_2O$ | 132.688 |
| 0.66 | $Ca_{0.66}SiO_{2.66}{\cdot}1.47H_2O$ | 123.576 |



https://doi.org/10.1180/minmag.2015.079.2.20 Published online by Cambridge University Press

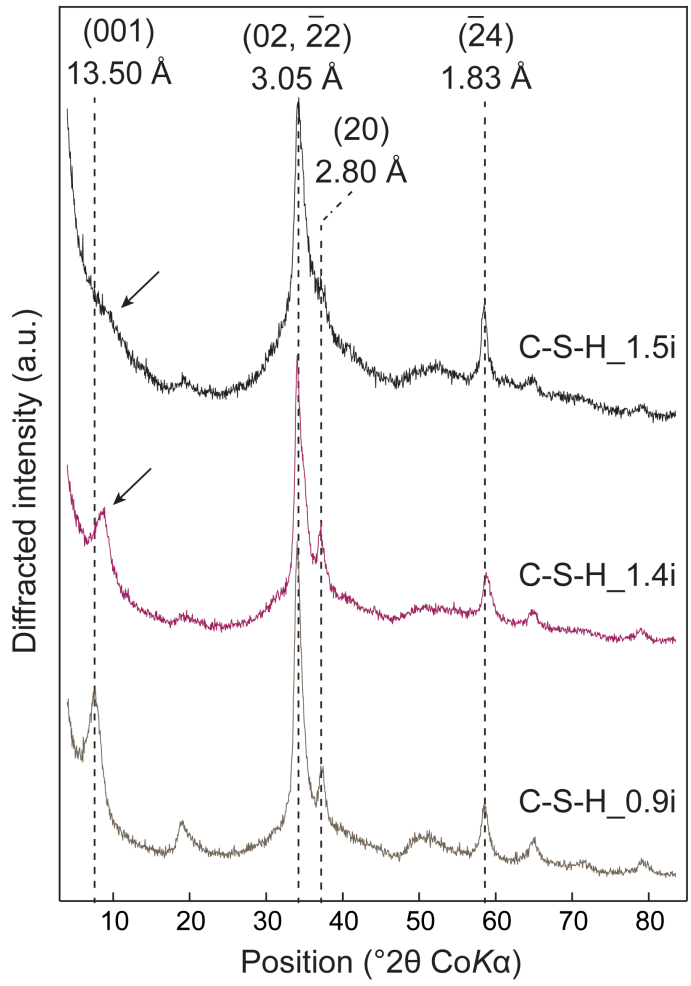


FIG. 2. XRD patterns of initial C-S-H (CSH_1.5i, CSH_1.4i and CSH_0.9i, from top to bottom). Vertical dotted lines indicate the main diffraction maxima from C-S-H, which are indexed following the structure model of Grangeon *et al.* (2013*b*). Arrows point out the main differences between all XRD patterns.

(Ca > 99%) and electron diffraction (interreticular distances of 3.04 Å and 1.61 Å). Vaterite, an unstable type of calcium carbonate, is also observed in CSH_1.4i material (Fig. 3). The mineral is characterized by diffraction maxima at 3.20 Å and 2.70 Å. TEM observations indicate that the mineral is weakly crystallized and intimately mixed with C-S-H particles. According to Šauman (1971), carbonation of C-S-H leads to the formation of vaterite. The origin of the carbonate is uncertain – simultaneously synthesized with C-S-H or C-S-H carbonation before its storage in the glove-box. No phases other than C-S-H have been observed in the CSH_0.9i sample. Electron diffraction analyses performed on C-S-H (Fig. 3) confirm the cryptocrystalline nature of the mineral: two diffraction rings at 2.85 Å and 3.11 Å are identified, in agreement with XRD patterns (Fig. 2). As opposed to estimations undertaken with EPMA, C/S estimations from TEM/EDX measurements were undertaken on positively identified C-S-H particles (i.e. absence of secondary phases) and led to the determination of C/S ratios assumed to be representative of C-S-H particles free of impurities (Table 2).



https://doi.org/10.1180/minmag.2015.079.2.20 Published online by Cambridge University Press

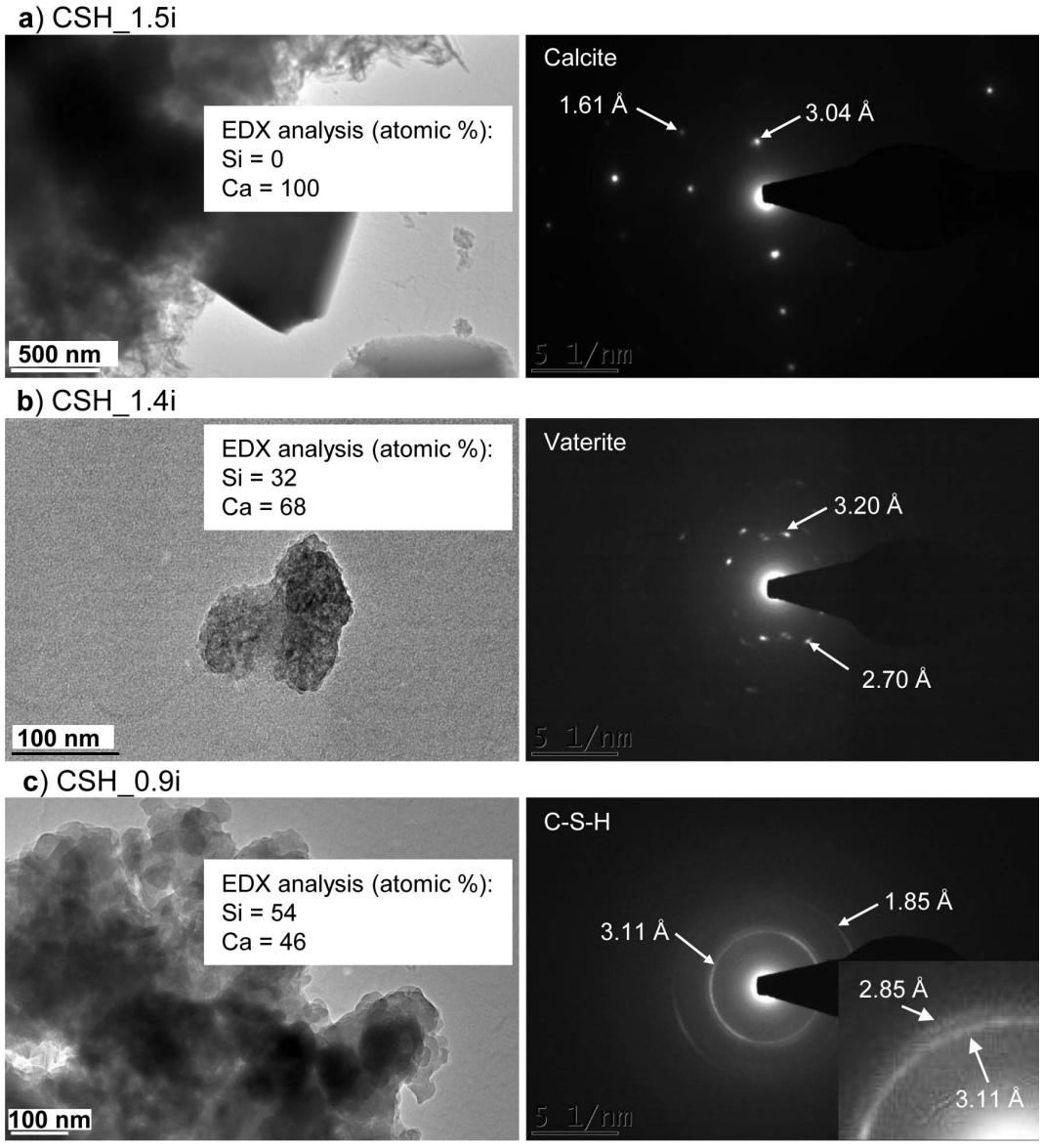


FIG. 3. TEM images of C-S-H samples before dissolution experiments (left column) and corresponding electron diffraction patterns (right column). (*a*) Sample CSH_1.5i shows the presence of well crystallized calcite; (*b*) sample CSH_1.4i shows a carbonation of C-S-H (formation of vaterite); and (*c*) shows sample CSH_0.9i where no phase other than C-S-H has been observed.

The TGA obtained on the three unreacted samples are shown in Fig. 4. Data were smoothed by fitting a tensioned spline to the experimental data, with spline tension set to $9 \times 10^{-4}$, for DTG calculations. Examination of both DTG and heat flows indicated that CSH_1.5i contains CH associated with traces of calcite, CSH_1.4i incorporates CH, vaterite and traces of calcite, whereas CSH_0.9i is almost a pure C-S-H phase. TGA results enabled us to estimate the percentage



https://doi.org/10.1180/minmag.2015.079.2.20 Published online by Cambridge University Press

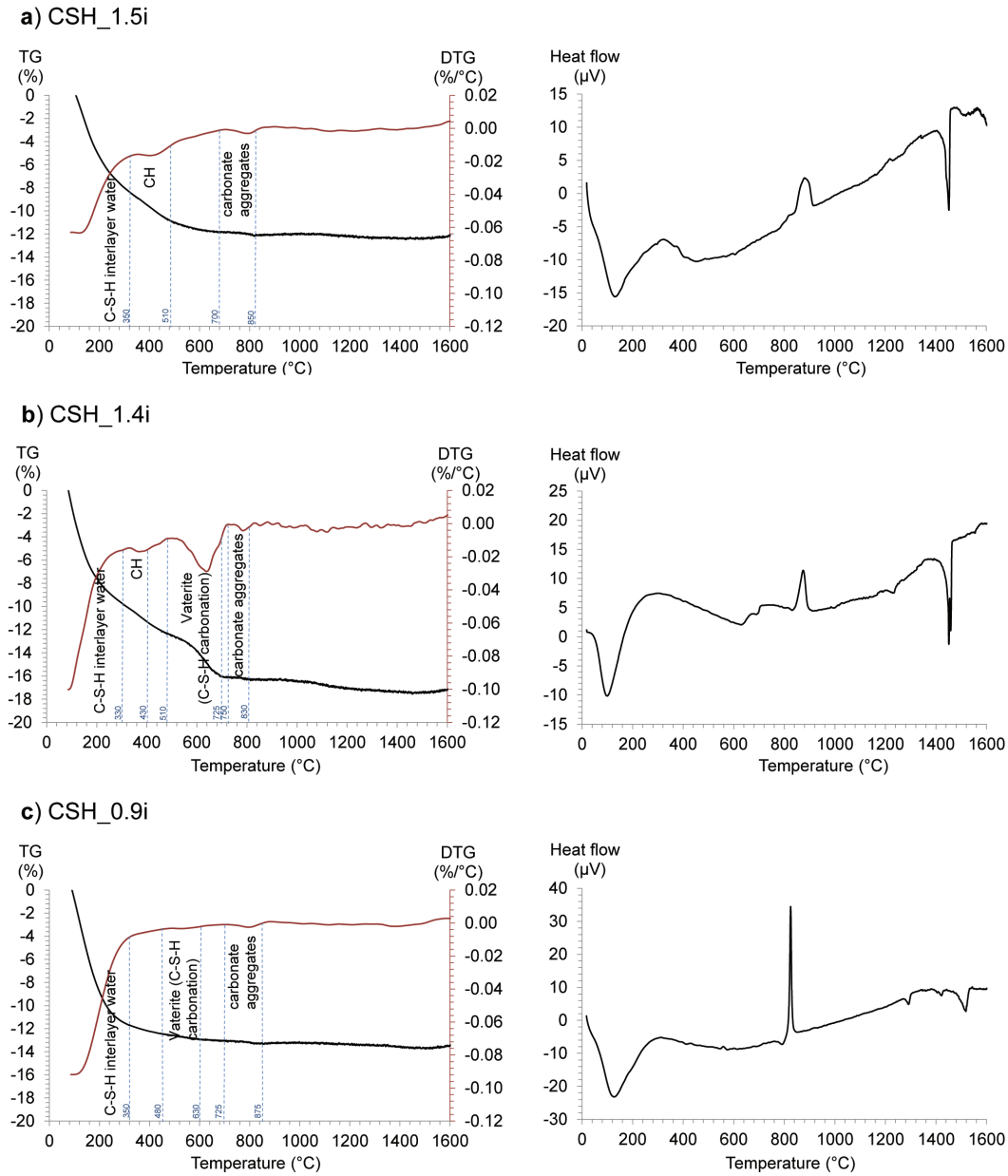


FIG. 4. TGA of CSH_1.5i, CSH_1.4i and CSH_0.9i, from top to bottom, before dissolution experiments. Left column: TGA (left *y* axis and solid black line) and corresponding derivative values (right *y* axis and solid red line) data. Right column: DSC data.

of accessory phases (Table 2). Initial stoichiometric ratios of C-S-H were assumed to be those obtained from TGA experiments. It is noteworthy that these phases were scarcely detectable, if at all, by XRD which suggests a cryptocrystalline nature. Also, such impurities could not be investigated by methods traditionally used to study the structure of C-S-H, in particular silicon nuclear magnetic resonance (Si NMR – e.g. Cong and Kirkpatrick, 1996). This highlights



https://doi.org/10.1180/minmag.2015.079.2.20 Published online by Cambridge University Press

the necessity of using methods such as those employed in the present study to obtain detailed insights into the nature of impurities that can be mixed intimately with C-S-H.

### *Discussion on the nature of the impurities*

The TGA and chemical data show consistently that CSH_1.4i and CSH_1.5i have structural C/S ratios of ~1.22 which is significantly lower than their bulk C/S ratios.

From TGA, the difference between bulk and structural Ca/Si ratios is due to the presence of impurities, namely calcium carbonate and CH. XRD shows that the only impurity that could be inferred to be present is a cryptocrystalline calcite. CH was not detected. In this case, therefore, CH is not crystallized portlandite *sensu stricto*, because this would have been recognized by, at least, an intense Bragg peak at ~2.63 Å (39.96º2θ) in the XRD pattern. Even low concentrations would have been detected because of the greater intensity of diffraction by crystalline phases compared to turbostratic phases. On the other hand, CH might be present as an amorphous product with a stoichiometry equal to that of $Ca(OH)_2$ or in a nanocrystalline form, in which case, it would be scarcely detectable by XRD because its intensity would be distributed over a large angular range. According to Chen *et al.* (2010), intimate mixes of C-S-H and CH crystals can adopt two main configurations: microcomposite, with CH precipitating outside C-S-H porosity, and nanocomposite, with CH precipitating within C-S-H porosity and thus supposedly intimately mixed with the C-S-H structure. In the hydrated cement pastes studied by Chen *et al.* (2010), nanocomposite is assumed to be favoured when water and space are deficient. Because the typical size of C-S-H interlayer space (i.e. porosity) is ~11 Å along **c*** and ~7 Å in the **ab** plane, CH precipitating in this region will probably be too small to produce any detectable XRD signal. Therefore, in our present study, CH and C-S-H are certainly present in the form of the nanocomposite structure described by Chen *et al.* (2010). The validity of this assumption cannot be checked by looking at TGA (and DSC) curves and comparing the temperatures of CH decomposition in this present study with pure portlandite, because of numerous uncertainties, e.g. the influence of nanocrystallinity on the thermal stability of this phase and the influence of potential structural linkage between CH nanocomposites located in C-S-H interlayers and C-S-H itself. However, additional agreement between this model and our results comes from the observed increase in CH content (Table 2) with decreasing structural water (deduced from the weight loss between the ambient temperature and the lower boundary for CH destabilization) which is 12%, 10% and 9% for CSH_0.9i, CSH_1.4i and CSH_1.5i, respectively. These values are in close agreement with those determined previously by Kim *et al.* (2013) on two C-S-H samples also equilibrated at 11% relative humidity and with XRD patterns typical of pure C-S-H. They found that C-S-H with a C/S ratio of 0.73 and 1 contained 9 wt.% and 11 wt.% water, respectively. Therefore, when more nanocrystalline CH is present in C-S-H interlayer space, less space is available for water. When C-S-H porosity is filled with CH (at high C/S ratio) the formation of C-S-H/CH microcomposite should be favoured. Because CH crystallizing outside of the C-S-H porosity obviously has more available space, especially in our case where C-S-H was synthesized using aqueous chemistry, it should have a much larger crystallite size (Chen *et al.*, 2010), may not be structurally linked to C-S-H (as possibly opposed to nanocomposites) and should then be detectable by XRD. This is in agreement with the results of Grangeon *et al.* (2013*a*), who, using literature data, demonstrated that C-S-H with a C/S ratio <~1.25 could be described as nanocrystalline tobermorite, and who observed the almost systematic presence of a portlandite signal in the XRD patterns of synthetic samples having a Ca/Si ratio >~1.5. These results also support the model of Richardson (2004, 2008), who suggested that the entire structural variation of C-S-H as a function of the Ca/Si ratio can be described using tobermorite and CH.

Assuming that the C-S-H/CH model is valid, with C-S-H resembling nanocrystalline and turbostratic tobermorite, the maximum C/S ratio that can be reached before CH starts to nucleate can be estimated. It would correspond to a tobermorite-like structure with all Si bridging tetrahedra from silicate chains omitted, and interlayer Ca increased to the maximum theoretical value determined by Merlino *et al.* (2001) and would be equal to 1.25, in close agreement with values determined in the present study for C-S-H_1.4i and C-S-H_1.5i. A C-S-H structural ratio of 1.24 in a sample having a bulk ratio of 1.5 has also been observed by Kim *et al.* (2013), who also used TGA, and ~1.25 may actually be the



https://doi.org/10.1180/minmag.2015.079.2.20 Published online by Cambridge University Press

upper limit for C-S-H C/S ratio, at least for samples synthesized by $CaO/SiO_2$ aqueous chemistry. It is in agreement with the results of Cong and Kirkpatrick (1996) who noticed, using charge-balance calculations, that C-S-H with a bulk C/S ratio >~1.3 had an excess of Ca, which can be attributed to CH. The structure of the product named CH is, however, unclear and may change with bulk C/S ratio: in the case of nanocomposites defined by Chen *et al.* (2010), C-S-H and CH may be structurally linked, whereas in the case of microcomposites, the bulk sample may contain discrete portlandite.

## Chemical evolution during C-S-H dissolution

### *Fluid chemistry evolutions*

Output pH values were always larger than input values (Fig. 5). High initial pH values obtained with the CSH_1.5 experiment are consistent with high CH content (Table 2). In all of the flow-through experiments, Ca concentrations decreased continuously with time (Fig. 5). The high initial Ca concentrations are due to both the rapid dissolution of CH impurities and/or the release of exchangeable cations. Si concentrations seemed to stabilize between 30 and 80 h. However, no unambiguous steady state could be determined because of the solid composition and reacting mass evolutions. The results are given in detail in the Appendix (deposited at www.minersoc.org/pages/e_journals/dep_mat_mm.html).

After 80 h, both the strong decrease in the silicon concentration and the absence of any difference between input and output pH values indicate a total dissolution of CSH_1.5i. Except for the residual phases (probably insoluble) that were found on the reactor filter, no material was retrieved from the filtered reactor suspension at the end of the experiment (Table 1).

Silicon concentrations were always below the amorphous silica solubility limit (*PHREEQC* calculations using the *THERMODDEM* database – Blanc *et al.*, 2012; Parkhurst and Appelo, 1999). The formation of this mineral during dissolution experiments was therefore excluded.

### *C/S evolution*

As discussed previously, knowledge of the mineral stoichiometry is essential for the determination of reaction rates. The analytical procedure used for the estimation of C/S ratios is summarized in Table 4. Ratios obtained for

TABLE 4. Analytical procedure used for the determination of C/S ratios as function of time.

| | Description | Initial (starting material) | During experiment | Final (recovered material) |
|---|---|---|---|---|
| Solid | Bulk C/S ratio | EPMA (direct measurement) | – | – |
| | Stoichiometric C/S ratio | TEM/EDX (direct measurement)<br>TGA/DSC (indirect estimation) | TEM/EDX (direct measurement)<br>Solution chemistry (indirect estimation) | TEM/EDX (direct measurement)<br>EPMA* (direct measurement)<br>Solution chemistry (indirect estimation) |
| Solution | C/S ratio of output concentrations | ICP-AES (direct measurement) | ICP-AES (direct measurement) | ICP-AES (direct measurement) |

* Assuming a total dissolution of eventual impurities.



https://doi.org/10.1180/minmag.2015.079.2.20 Published online by Cambridge University Press

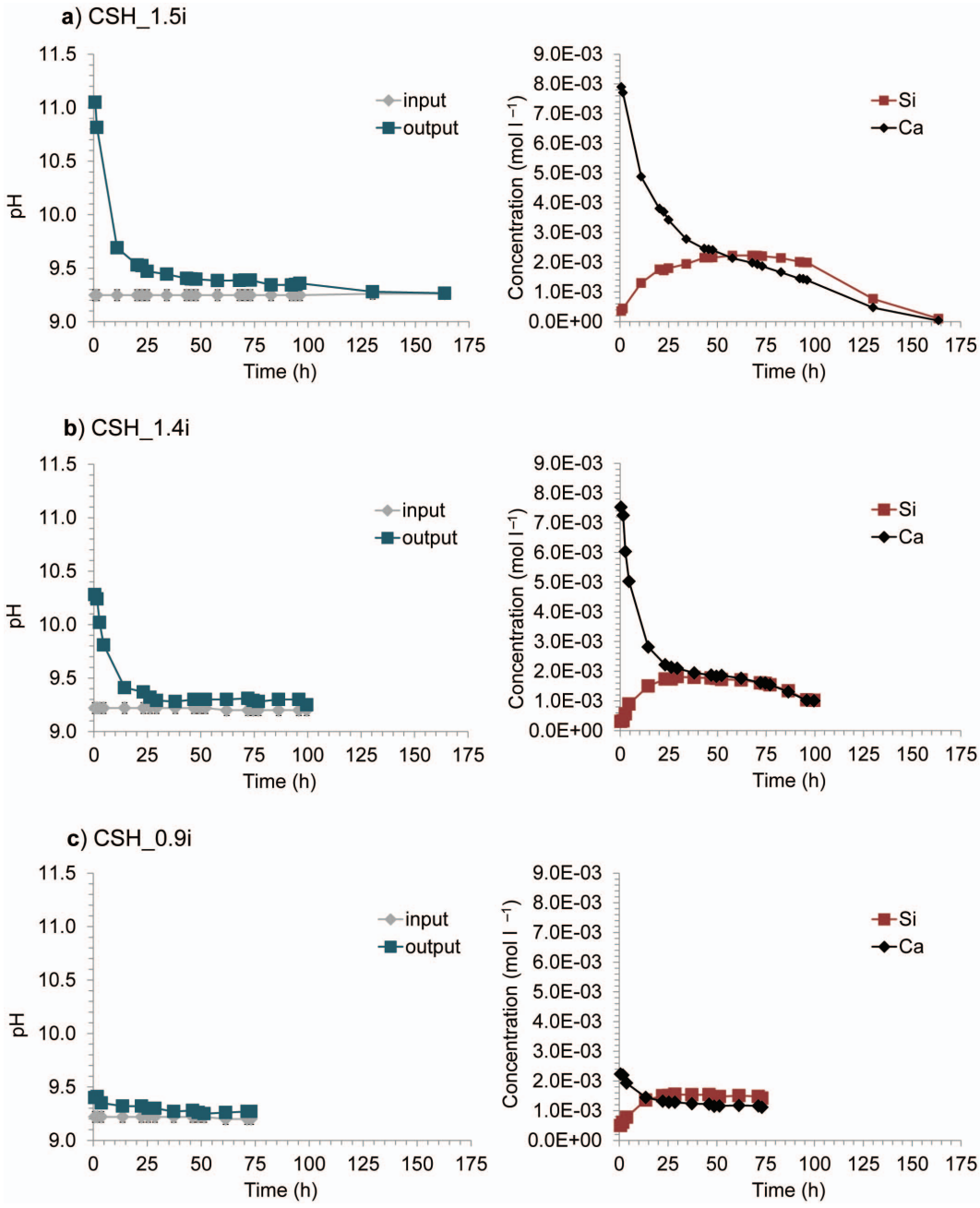


FIG. 5. Fluid chemistry evolution as a function of time for CSH_1.5i, CSH_1.4i and CSH_0.9i, from top to bottom. Left column: pH value, measured in the input (grey solid line and filled grey diamonds) and the output (green solid line and filled green squares) solutions. Right column: Si (red solid line and filled red squares) and Ca (black solid line and filled black diamonds) concentrations measured in the output solution. Ca, Si and pH detection limits were $1.2 \times 10^{-5}$ M, $8.3 \times 10^{-6}$ M and 0.05, respectively. In all experiments, the symbols are data points and the lines are intended to be a guide for the eye.



https://doi.org/10.1180/minmag.2015.079.2.20 Published online by Cambridge University Press

solutions and solids as a function of time are compared in Fig. 6. Initial C/S ratios of solids were calculated from EPMA (bulk C/S ratios), TGA/DSC (C-S-H stoichiometric C/S ratios) and TEM/EDX (C-S-H stoichiometric C/S ratios). The evolution of the C-S-H stoichiometry during the whole course of the experiment was calculated using solution chemistry as well as from punctual solid sampling followed by TEM/EDX analyses.

Results reported on Fig. 6 are divided into three steps which are summarized in Table 5. The first step is only observed in experiments using CSH_1.5i and CSH_1.4i. Calculation of initial C/S ratios of the solutions (dotted curves on Fig. 6) gave high values (up to 24.7 and 22.3 for CSH_1.4 and CSH_1.5, respectively; data not shown on Fig. 6) which decreased sharply during the first hours of alteration. Such decrease,

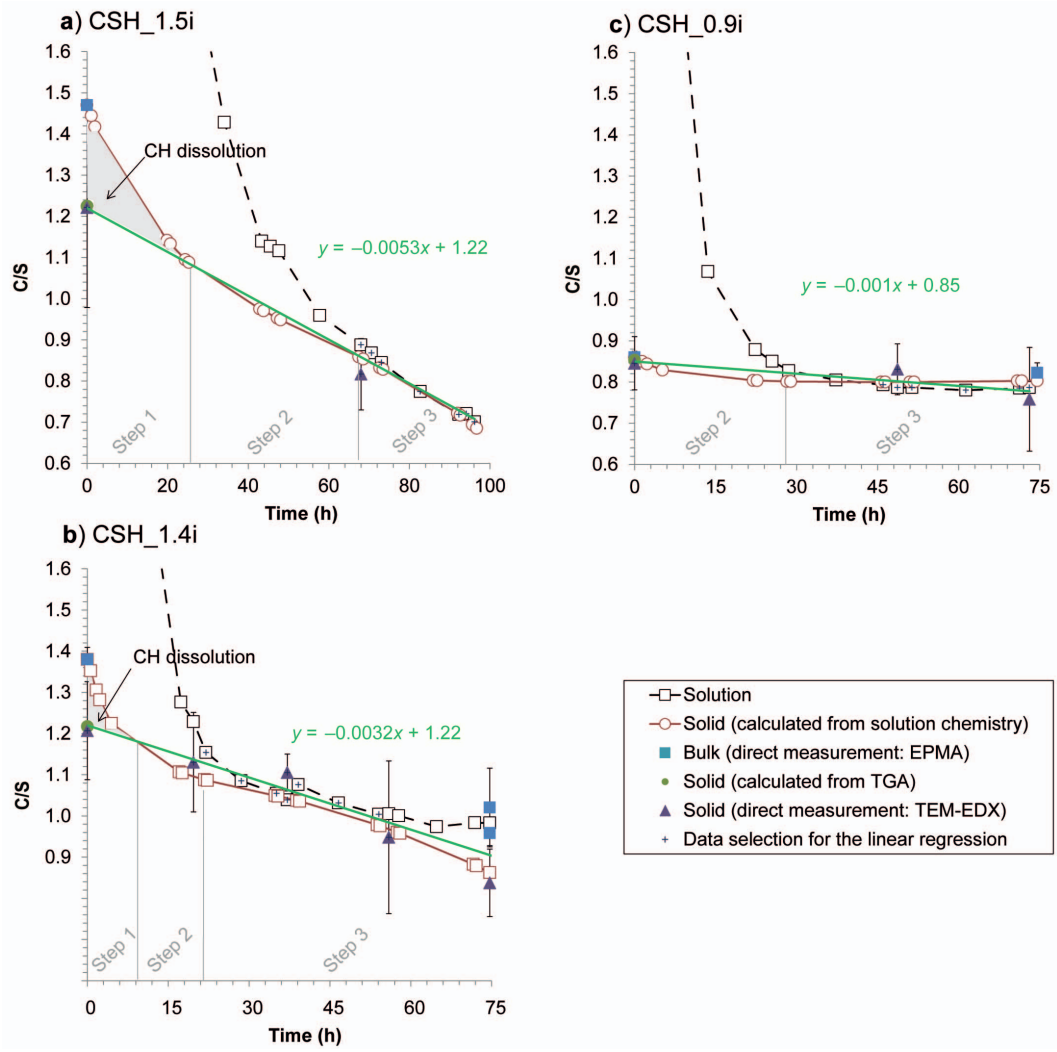


FIG. 6. C/S ratios of solutions and solids in experiments employing CSH_1.5i (*a*), CSH_1.4i (*b*) and CSH_0.9i (*c*). Data obtained in solution are open black squares and dotted black line. Composition of the solid is estimated from solution chemistry (open red square and solid red line), from EPMA (filled blue square), TGA (filled green circle) and from TEM-EDX (filled purple triangle). Green solid line is a linear regression from grey crosses. Identified steps are discussed in the text and summarized in Table 5. In all experiments, the symbols are data points and the lines are intended to be a guide for the eye.



https://doi.org/10.1180/minmag.2015.079.2.20 Published online by Cambridge University Press

TABLE 5. Characteristics and interpretations of different dissolution steps observed on Fig. 6.

| | Characteristics | Interpretations | Remarks |
|---|---|---|---|
| Step 1 | High pH and Ca concentrations (Fig. 5)<br>Increase of Si concentrations (Fig. 5) | CH dissolution and Ca/Na exchange | Calculation of dissolution rates impossible |
| Step 2 | High Ca concentrations (Fig. 5)<br>Weak variation of pH and Si concentrations (Fig. 5) | Ca/Na exchange | Dissolution rates calculated from Si concentrations |
| Step 3 | Weak variation of pH as well as of Ca and Si concentrations (Fig. 5) | Close to stoichiometric dissolution (Fig. 6) | Dissolution rates calculated from Si and Ca concentrations |

associated with the highly preferential release of Ca and high pH values (Fig. 5), strongly suggests CH dissolution in the first 20 h of alteration. Ca/Na exchange certainly also contributes to the preferential releases of Ca, but would not induce a pH increase, and thus cannot explain the observed evolution during the first hours.

From the second step, the evolution of the C/S of pure C-S-H phases, i.e. free from CH (from the beginning for CSH_0.9 and after 20 h for CSH_1.5i and CSH_1.4i), can be modelled by linear regression (solid green lines on Fig. 6). The function was determined from measurements performed on both solutions and solids. The evolution of the solid C/S ratio estimated from solution chemistry (solid red curves on Fig. 6) validates the proposed law. Step 2 is characterized by a preferential release of Ca. Assuming an absence of CH supported by low pH values reported on Fig. 5, large Ca concentrations result from Ca/Na exchange reactions. Note that the residence time of water in the reaction vessel was ~2.6 ± 0.2 hours; therefore the apparent excess cannot be attributed to dilution effects of Ca released during the first steps. Considering the Ca preferential release, dissolution rates can only be calculated from Si concentrations.

In the third step, output concentrations reflect C-S-H stoichiometry. In the only sample where congruency was clearly observed (CSH_0.9), the C/S ratio reached ~0.83 in full agreement with previous studies (Baston *et al.*, 2012; Harris *et al.*, 2002; Trapote-Barreira *et al.*, 2014; Vieillard and Rassineux, 1992). Such behaviour could not be validated in other samples. Moreover, as variations in C-S-H compositions are observed in CSH_1.5 and CSH_1.4 experiments, a congruent dissolution cannot be considered *sensu stricto*. However the C/S ratios calculated from output concentrations (dotted curves in Fig. 6) are very close to the stoichiometric C/S of the C-S-H after 50 h of experiments. Therefore dissolution rates can be estimated using both Ca and Si output concentrations.

Solid analyses undertaken on CSH_1.4f revealed discrepancies in C/S determination. EPMA at the millimetre scale (Fig. 7) led to a C/S of 1.02 ± 0.10 ($n$ = 40), whereas this ratio was 0.96 ± 0.03 ($n$ = 27) when isolated particles were analysed. From the TEM/EDX experiment performed on suspended matter, this ratio was 0.84 ± 0.08 ($n$ = 20). The higher ratio obtained using EPMA argues for the presence of Ca impurities, as EDX analyses were undertaken on positively identified C-S-H particles and should therefore be more representative of CSH_1.4f stoichiometry, as shown by its very good agreement with C/S calculated from solution chemistry (red curve on Fig. 6*b*). Taking into account the rapid reaction rate of CH (Galı *et al.*, 2001; Halim *et al.*, 2005; López-Arce *et al.*, 2010), any remaining accessory mineral is probably vaterite or calcite (initially identified in CSH_1.4i).

### *Dissolution rates*

Dissolution rates are plotted as a function of C/S ratios in Fig. 8. Reaction rates obtained using CSH_1.5i and CSH_1.4i (i.e. for initial C/S of 1.22) are very similar. The slight differences might be due to a stronger carbonation of CSH_1.4i (Fig. 4*b*). C-S-H solubility is known to increase with the C/S ratio (Blanc *et al.*, 2010).



https://doi.org/10.1180/minmag.2015.079.2.20 Published online by Cambridge University Press

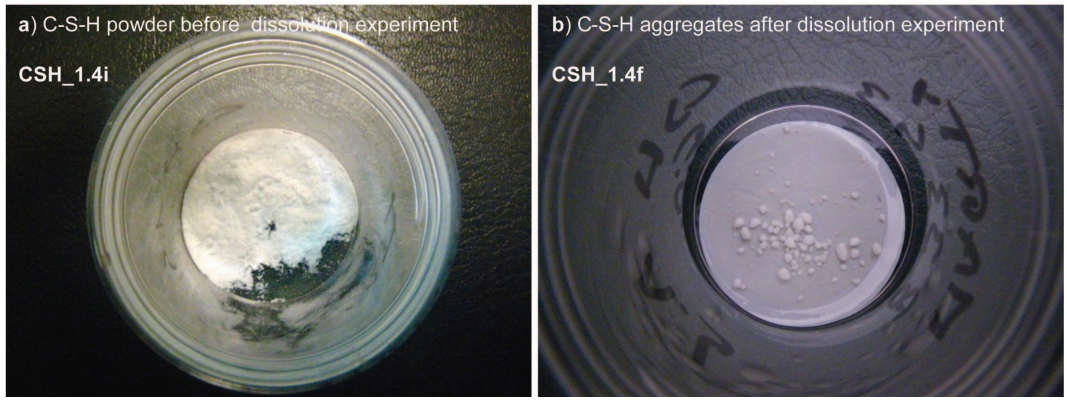


FIG. 7. Aggregates formed during dissolution experiments (CSH_1.4 experiment). Left: CSH_1.4i, right: CSH_1.4f.

Therefore, the effects of pH on the dissolution rates obtained for the initial C/S ratios of 0.85 (CSH_0.9i) and 1.22 (CSH_1.5i and CSH_1.4i) are probably different.

Far-from-equilibrium dissolution kinetics at pH 9.2 and room temperature are expressed as a function of the C/S ratio:

$$R_{CSH\_1.5}\ (\text{mol m}^{-2}\ \text{s}^{-1}) = (-1.33 \times 10^{-10})\text{C/S} + 1.77 \times 10^{-10} \quad (17)$$

$$R_{CSH\_1.4}\ (\text{mol m}^{-2}\ \text{s}^{-1}) = (-1.60 \times 10^{-10})\text{C/S} + 2.211 \times 10^{-10} \quad (18)$$

$$R_{CSH\_0.9}\ (\text{mol m}^{-2}\ \text{s}^{-1}) = (-1.76 \times 10^{-10})\text{C/S} + 1.69 \times 10^{-10} \quad (19)$$

Experimental data are modelled well using these linear regressions (Fig. 8). Our kinetic data are in good agreement with the tobermorite dissolution rate reported by Schweizer (1999) in similar conditions ($4.22 \times 10^{-11}$ mol m$^{-2}$ s$^{-1}$ at pH 9 and 25ºC). Considering the kinetic constant at pH 10.5 to 11 extracted from Trapote-Barreira *et al.* (2014) on C-S-H ($3.21 \times 10^{-11}$ mol m$^{-2}$ s$^{-1}$) as well as experiments performed by Schweizer (1999) on C-S-H, tobermorite and xonotlite, the dissolution rate decreases in basic conditions.

## Mineralogical characterization of reacting material

### *Alteration products*

CSH_1.5f was subjected to the longest alteration time and C-S-H was assumed to be fully dissolved. The XRD pattern of the final alteration product is shown in Fig. 9. The remaining solid is an assemblage of calcite, fluorapatite, quartz, brucite, aluminium silicate, magnesium aluminium hydroxide hydrate and CH, which certainly formed during sample drying. Because the sum of all of these phases weighed <0.5% of the initial mass (which explains why they were not detectable on the initial XRD patterns), they are unlikely to have influenced the solution chemistry. On the other hand, XRD patterns for CSH_1.4f and CSH_0.9f, which had less solution contact time, are still typical for C-S-H. Compared to fresh samples (CSH_1.4i and CSH_0.9i), the most obvious difference is a shift towards higher angular values (i.e. smaller *d*-spacing), which cannot be attributed to a measurement artefact (e.g. sample height) because rutile Bragg peaks are located at their theoretical value. This indicates a decrease in the layer-to-layer distance with alteration, whereas the shift of *hk* bands indicates a decrease in the apparent lattice parameters in the **a**–**b** plane (layer plane). Using the structure model from Grangeon *et al.* (2013*a*), *a* and *b* were equal to 6.731 Å and 7.371 Å in C-S-H_0.9i and 6.770 Å and 7.371 Å in C-S-H_1.4i. At the end of the alteration experiment, *a* decreased to 6.705 Å in C-S-H_0.9f and 6.705 Å in C-S-H_1.4f, whereas *b* decreased to 7.323 Å in C-S-H_0.9f and C-S-H_1.4f.

### *Mineralogical evolution during alteration*

Based on the chemical composition of the solution, two main dissolution phenomena take place as a function of alteration time. First of all, dissolution is non-stoichiometric, with preferential Ca release, which cannot be attributed fully to preferential dissolution of impurities because this



https://doi.org/10.1180/minmag.2015.079.2.20 Published online by Cambridge University Press

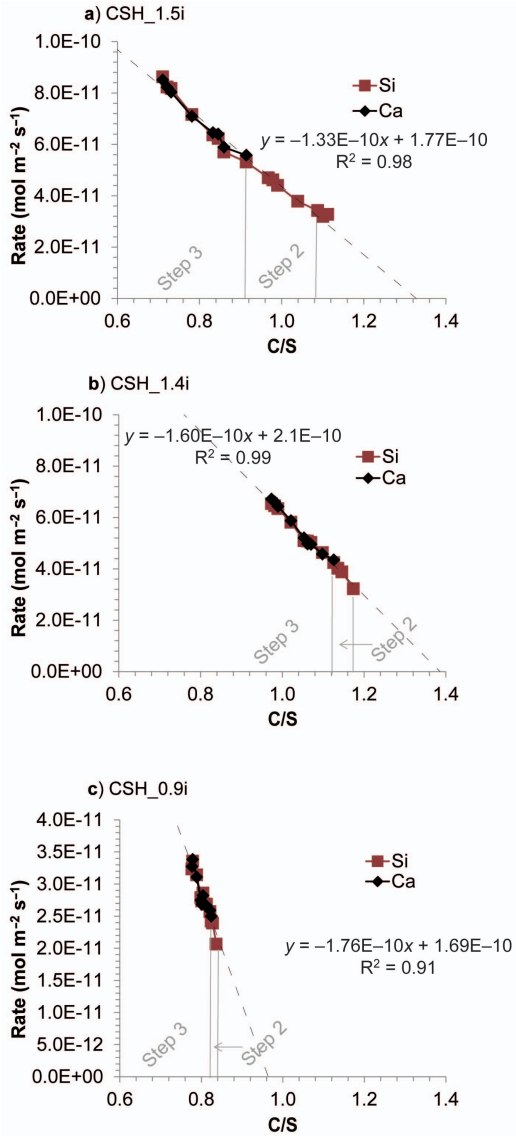


FIG. 8. Dissolution rate as a function of the C/S ratio at pH 9.2 and room temperature, for samples CSH_1.5i, CSH_1.4i and CSH_0.9i, from top to bottom. In each experiment, filled red squares and solid red lines are calculated from Si concentration in the solution and filled black diamonds and the solid black line are calculated from the Ca concentration. In all experiments, the grey dotted line is the linear regression to the data, the symbols are data points and the lines are intended to be a guide for the eye.

phenomenon is also observed in the CSH_0.9 experiment (i.e. using a pure C-S-H phase). Thereafter, dissolution is stoichiometric. This can be interpreted in structural terms, using TGA, TEM and XRD data. In C-S-H, calcium has two main crystallographic sites: layer and interlayer. The preferential release of Ca observed during the first step is certainly due to the dissolution of impurities, and then to the release of interlayer Ca because layer Ca is strongly bound and is certainly not released in early stages of alteration. XRD provides clues to the preferential release of interlayer Ca, through the decrease in the layer-to-layer distance which certainly results from the replacement of Ca by Na from the input solution (Bach *et al.*, 2013; Sugiyama, 2008). In particular, Bach *et al.* (2013) observed, on a C-S-H sample with a C/S ratio of 0.83, a decrease in the layer-to-layer distance with increasing Na concentration in the solution: layer-to-layer distance was 13.98 Å after equilibration in a Na-free solution as compared to a position of the (001) reflection of 13.50 Å in sample C-S-H_0.9i. After equilibration in a solution containing 28.14 mmol $l^{-1}$ of Na, Bach *et al.* (2013) observed that the layer-to-layer distance reduced to 12.79 Å, as compared to a position of the (001) reflection at 12.67 Å in sample C-S-H_0.9f, which was in contact with a solution having a Na concentration of 20 mmol $l^{-1}$. Preferential depolymerization from the silicate chains, is another possible hypothesis to explain the decrease in layer-to-layer distance because it would reduce the occupancy of the interlayer space and could thus allow a decrease of the layer-to-layer distance, is unlikely because no preferential release of Si is observed throughout the course of all three dissolution experiments. The second dissolution step, marked by a close to stoichiometric release of Ca and Si, mainly results from the dissolution of C-S-H layers, which undoubtedly proceeds from the outer layer to the inside of the particles. This is supported by examination of XRD patterns. Upon dissolution, the apparent in-plane *a* and *b* lattice parameters decrease. This might indicate either an actual contraction of the structure or layer bending and/or corrugation, as has been reported for nanocrystalline Mn oxides (Manceau *et al.*, 2013) and nanocrystalline layered double hydroxides (Hadi *et al.*, 2014). TEM would seem to indicate layer bending and corrugation, as crystals appear to be curved (Fig. 10), which is probably caused by the decrease in particle size and thus increase of surface energy.



https://doi.org/10.1180/minmag.2015.079.2.20 Published online by Cambridge University Press

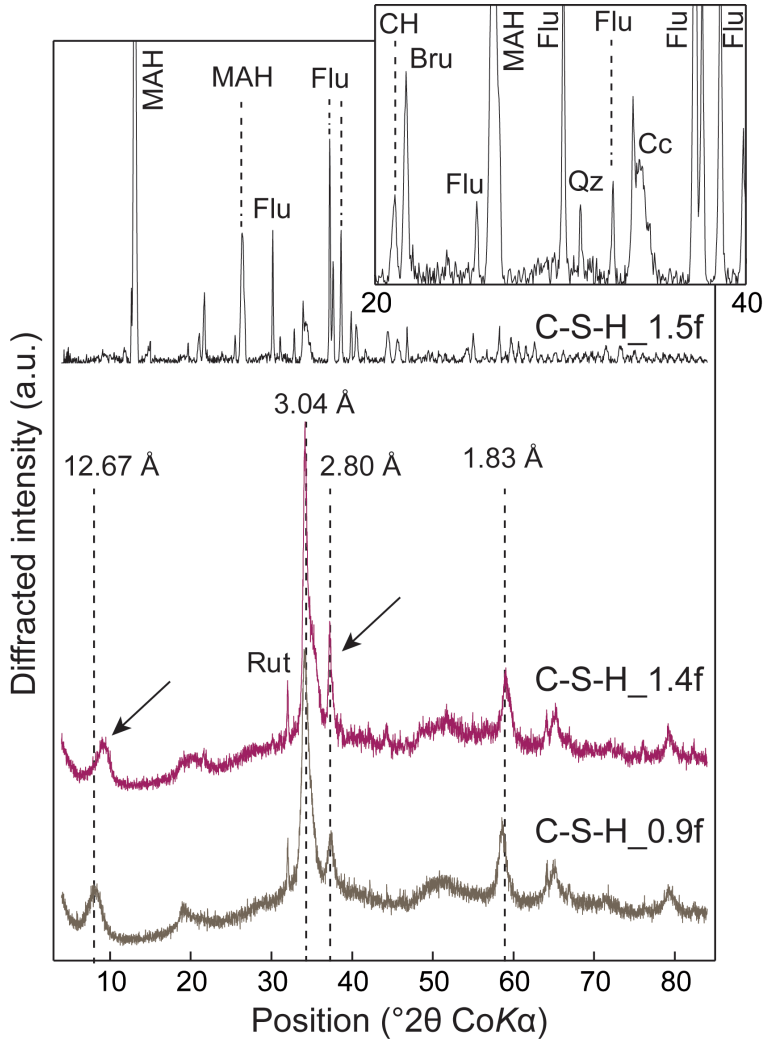


FIG. 9. XRD patterns of final alteration products (CSH_1.5f, CSH_1.4f and CSH_0.9f, from top to bottom). Inset in top right is a detail of the XRD pattern from CSH_1.5f, between 20 and 40º2θ. MAH, Flu, CH, Bru, Qz and CC identify diffraction maxima from magnesium aluminium hydroxide hydrate, fluoroapatite, calcium hydroxide, brucite, quartz and calcite, respectively. In XRD patterns from CSH_1.4f and CSH_0.9f, vertical dotted lines show the positions of the main diffraction maxima commonly reported for C-S-H, arrows indicate the main differences between the two XRD patterns and Rut is the Rutile diffraction peak.

### *Structural similarity between C-S-H and tobermorite inferred from the composition of the interlayer space*

Assuming that the preferential release of Ca at the beginning of the CSH_0.9i dissolution experiment is a result of the preferential release of interlayer Ca, and using both chemical data and the results of TGA, we can calculate the composition of the interlayer, and in particular the interlayer water ($H_2O$) to Ca molar ratio. Water content (in moles per gram of C-S-H) is estimated from the weight loss between 0 and the lower boundary for CH decomposition (as estimated from TGA from CSH_1.4i and CSH_1.5i because CSH_0.9i does not contain CH). Interlayer Ca (in moles per gram of C-S-H) is estimated from the number of moles of Ca released during the first dissolution step,



https://doi.org/10.1180/minmag.2015.079.2.20 Published online by Cambridge University Press

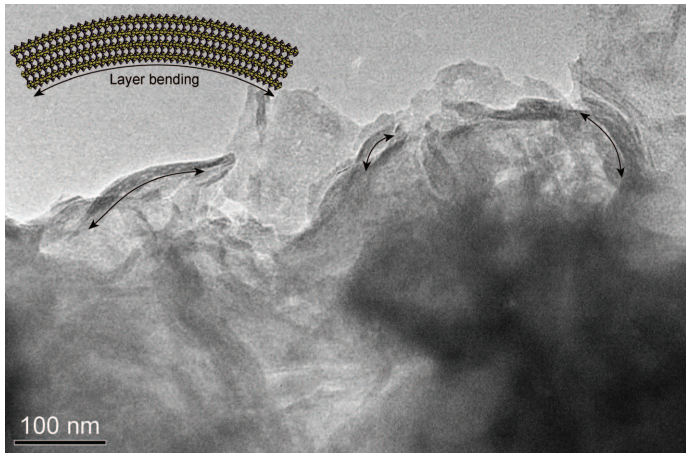


FIG. 10. Illustration of C-S-H layer bending, using TEM observation of CSH_0.9f. Top left is a sketch of a C-S-H particle suffering from bending (yellow polyhedra and purple tetrahedra, respectively, represent layer Ca and Si coordination spheres – not to scale with regards to the TEM image). In the TEM image, arrows underline the most obvious bent C-S-H crystals.

taking into account the contribution of layer Ca through the concentration of aqueous Si and the mean C/S ratio during stoichiometric dissolution. This calculation can only be done for CSH_0.9 because of the presence of impurities in the two other samples, thus preventing an accurate quantification of interlayer Ca. The resulting interlayer $Ca/H_2O$ ratio is 10.5, which is similar to the ratio found in tobermorite MDO2 from the Urals, which contains interlayer Ca (Merlino *et al.*, 2001) and a $Ca/H_2O$ ratio of 12. This further confirms the close structural similarity between C-S-H and tobermorite and may indicate that water structuration in both phases is similar.

### *Implications for the modelling of cement degradation*

In the present study, three different samples with varying C/S ratios were studied; one C/S ratio was characteristic of C-S-H found in low-pH cement (C-S-H_0.9i; bulk C/S = 0.86), the two others from C-S-H found in Portland cement (C-S-H_1.4i and C-S-H_1.5i; bulk C/S = 1.38 and 1.47). The XRD patterns of all samples were similar to those of C-S-H found in hydrated cement pastes (e.g. Bach *et al.*, 2012; Garcia Calvo *et al.*, 2010; Schneider *et al.*, 2001), and the presence of nanometric CH intermixed with C-S-H was observed in the two samples with the largest C/S ratios, which confirms that the samples being studied here are representative of those formed during hydration of cement pastes (the presence of nanometric CH in hydrated cement pastes was demonstrated by e.g. Allen *et al.*, 2007 and Chen *et al.*, 2010). Thus, kinetics law obtained in the present study for C-S-H of different C/S ratios are relevant to the understanding and modelling of cement degradation in mild basic conditions that can for example by reached at cement/clay interfaces or in granitic rocks (Garcia Calvo *et al.*, 2010; Marty *et al.*, 2009). It was found that congruent dissolution was achieved at a C/S ratio of 0.8. Assuming that the samples after alteration no longer contain interlayer Ca, this would correspond to a tobermorite-like structure with half of the bridging Si tetrahedra from the wollastonite-like chains omitted. Further work is necessary to assess the validity of this hypothesis. One area of investigation would be to see if C-S-H with such a ratio displays "normal" or "anomalous" (Merlino *et al.*, 2001) behaviour upon heating, to clarify if this phase contains interlayer Ca. Another logical follow-up of our present work would be the study of alteration of other cement components under the same conditions, and then of cement pastes, to contribute to a better understanding of the interaction between the different cement components during alteration.

## Conclusion

The alteration of C-S-H was studied with flow-through experiments (25ºC and pH 9.2) performed



https://doi.org/10.1180/minmag.2015.079.2.20 Published online by Cambridge University Press

on three different materials. The C/S ratios of the initial materials decreased because C-S-H phases are unstable under the present experimental conditions (far-from-equilibrium). The principal difficulty was measuring C/S evolution (i.e. mineral composition) during experiments to determine dissolution rates. This difficulty is partially compensated for by the simplicity of the structural formula; the limited number of constituent elements facilitates mass-balance calculations. Flow-through experiments combined with physical (TGA/DTA), mineralogical (XRD) and chemical (EPMA, TEM/EDX, ICP-AES) analyses are an excellent tool for evaluating C-S-H alteration. More specifically, the following conclusions can be drawn:

(1) The stoichiometric C/S ratios of the samples studied do not exceed 1.25, which is the upper limit that can be obtained using the tobermorite structure model, omitting all bridging tetrahedra and increasing the occupancy of interlayer Ca to the maximum value defined by Merlino *et al.* (2001). At higher ratios, the systematic presence of CH is deduced from TGA/DSC. This is consistent with the tobermorite/CH model developed by Richardson (2004, 2008).

(2) The dissolution rate is a linear function of the stoichiometric C/S ratios of the material.

(3) All results indicate that tobermorite and C-S-H are structurally very similar.

(4) In agreement with Bach *et al.* (2013), it was shown that XRD is sensitive to interlayer cation exchange. From the literature on clay minerals, a promising way of investigating the C-S-H interlayer structure would be to perform oriented preparations and to analyse them by the means of the "multi-specimen approach" (e.g. Claret *et al.*, 2004; Drits *et al.*, 1997; Lanson *et al.*, 2009).

## Acknowledgements

This study is a part of the CARMEN project initiated, carried out and funded by the French Geological Survey (BRGM). The authors thank V. Jean-Prost, V. Ruffier and S. Ory for the XRD measurements, XRD sample preparation and TGA/DSC measurements. F. Claret (BRGM) is thanked for comments and suggestions and A. Kay Bourg for the improvement of the English in the manuscript. The authors are grateful to Pr. T. Sato (Hokkaido University) for providing C-S-H samples. This manuscript benefited from comments and suggestions of two anonymous reviewers.

## References

Allen, A.J., Thomas, J.J. and Jennings, H.M. (2007) Composition and density of nanoscale calcium-silicate-hydrate in cement. *Nature Materials*, **6**, 311–316.

Bach, T.T.H., Coumes, C.C.D., Pochard, I., Mercier, C., Revel, B. and Nonat, A. (2012) Influence of temperature on the hydration products of low pH cements. *Cement and Concrete Research*, **42**, 805–817.

Bach, T.T.H., Chabas, E., Pochard, I., Cau Dit Coumes, C., Haas, J., Frizon, F. and Nonat, A. (2013) Retention of alkali ions by hydrated low-pH cements: Mechanism and $Na^{+}/K^{+}$ selectivity. *Cement and Concrete Research*, **51**, 14–21.

Baston, G.M.N., Clacher, A.P., Heath, T.G., Hunter, F.M.I., Smith, V. and Swanton, S.W. (2012) Calcium silicate hydrate (C-S-H) gel dissolution and pH buffering in a cementitious near field. *Mineralogical Magazine*, **76**, 3045–3053.

Blanc, P., Bourbon, X., Lassin, A. and Gaucher, E.C. (2010) Chemical model for cement-based materials: Temperature dependence of thermodynamic functions for nanocrystalline and crystalline C–S–H phases. *Cement and Concrete Research*, **40**, 851–866.

Blanc, P., Lassin, A., Piantone, P., Azaroual, M., Jacquemet, N., Fabbri, A. and Gaucher, E.C. (2012) Thermoddem: A geochemical database focused on low temperature water/rock interactions and waste materials. *Applied Geochemistry*, **27**, 2107–2116.

Bonaccorsi, E., Merlino, S. and Taylor, H.F.W. (2004) The crystal structure of jennite, $Ca_9Si_6O_{18}(OH)_6{\cdot}8H_2O$. *Cement and Concrete Research*, **34**, 1481–1488.

Brunauer, S. (1962) Tobermorite Gel – The heart of concrete. *American Scientist*, **50**, 210–229.

Butcher, E.J., Borwick, J., Collier, N. and Williams, S.J. (2012) Long term leachate evolution during flow-through leaching of a vault backfill (NRVB). *Mineralogical Magazine*, **76**, 3023–3031.

Chen, J.J., Sorelli, L., Vandamme, M., Ulm, F.-J. and Chanvillard, G. (2010) A coupled nanoindentation/SEM-EDS study on low water/cement ratio portland cement paste: evidence for $C–S–H/Ca(OH)_2$ nanocomposites. *Journal of the American Ceramic Society*, **93**, 1484–1493.

Claret, F., Sakharov, B.A., Drits, V.A., Velde, B., Meunier, A., Griffault, L. and Lanson, B. (2004) Clay minerals in the Meuse-Haute Marne Underground Laboratory (France): possible influence of organic matter on clay mineral evolution. *Clays and Clay Minerals*, **52**, 515–532.

Cong, X. and Kirkpatrick, R.J. (1996) $^{29}Si$ and $^{17}O$ NMR investigation of the structure of some crystal-



https://doi.org/10.1180/minmag.2015.079.2.20 Published online by Cambridge University Press

line calcium silicate hydrates. *Advanced Cement Based Materials*, **3**, 133–143.

Drits, V.A., Lindgreen, H., Sakharov, B.A. and Salyn, A.S. (1997) Sequence structure transformation of illite-smectite-vermiculite during diagenesis of Upper Jurassic shales, North Sea. *Clay Minerals*, **35**, 351–371.

Galı, S., Ayora, C., Alfonso, P., Tauler, E. and Labrador, M. (2001) Kinetics of dolomite–portlandite reaction: Application to portland cement concrete. *Cement and Concrete Research*, **31**, 933–939.

Garbev, K., Bornefeld, M., Beuchle, G. and Stemmermann, P. (2008) Cell dimensions and composition of nanocrystalline calcium silicate hydrate solid solutions. Part 2: X-Ray and thermogravimetry study. *Journal of the American Ceramic Society*, **91**, 3015–3023.

Garcia Calvo, J.L., Hidalgo, A., Alonso, C. and Fernandez Luco, L. (2010) Development of low-pH cementitious materials for HLRW repositories: Resistance against ground waters aggression. *Cement and Concrete Research*, **40**, 1290–1297.

Gherardi, F., Audigane, P. and Gaucher, E.C. (2012) Predicting long-term geochemical alteration of wellbore cement in a generic geological $CO_2$ confinement site: Tackling a difficult reactive transport modeling challenge. *Journal of Hydrology*, **420–421**, 340–359.

Glasser, F.P. (2001) Mineralogical aspects of cement in radioactive waste disposal. *Mineralogical Magazine*, **65**, 621–633.

Grangeon, S., Claret, F., Lerouge, C., Warmont, F., Sato, T., Anraku, S., Numako, C., Linard, Y. and Lanson, B. (2013*a*) On the nature of structural disorder in calcium silicate hydrates with a calcium/silicon ratio similar to tobermorite. *Cement and Concrete Research*, **52**, 31–37.

Grangeon, S., Claret, F., Linard, Y. and Chiaberge, C. (2013*b*) X-ray diffraction: a powerful tool to probe and understand the structure of nanocrystalline calcium silicate hydrates. *Acta Crystallographica Section B*, **69**, 465–473.

Hadi, J., Grangeon, S., Warmont, F., Seron, A. and Greneche, J.-M. (2014) A novel and easy chemical-clock synthesis of nanocrystalline cobalt-iron bearing layered double hydroxides. *Journal of Colloid and Interface Science*, **434**, 130–140.

Halim, C.E., Short, S.A., Scott, J.A., Amal, R. and Low, G. (2005) Modelling the leaching of Pb, Cd, As, and Cr from cementitious waste using PHREEQC. *Journal of Hazardous Materials*, **125**, 45–61.

Harris, A.W., Manning, M.C., Tearle, W.M. and Tweed, C.J. (2002) Testing of models of the dissolution of cements – leaching of synthetic CSH gels. *Cement and Concrete Research*, **32**, 731–746.

Hoch, A.R., Baston, G.M.N., Glasser, F.P., Hunter, F.M.I. and Smith, V. (2012) Modelling evolution in the near field of a cementitious repository. *Mineralogical Magazine*, **76**, 3055–3069.

Houston, J.R., Maxwell, R.S. and Carroll, S.A. (2009) Transformation of meta-stable calcium silicate hydrates to tobermorite: reaction kinetics and molecular structure from XRD and NMR spectroscopy. *Geochemical Transactions*, **10**:1.

Kantro, D.L., Brunauer, S. and Weise, C.H. (1962) Development of surface in the hydration of calcium silicates. II. Extension of investigations to earlier and later stages of hydration. *The Journal of Physical Chemistry*, **66**, 1804–1809.

Kim, J.J., Foley, E.M. and Reda Taha, M.M. (2013) Nano-mechanical characterization of synthetic calcium–silicate–hydrate (C–S–H) with varying $CaO/SiO_2$ mixture ratios. *Cement and Concrete Composites*, **36**, 65–70.

Lanson, B., Marcus, M.A., Fakra, S., Panfili, F., Geoffroy, N. and Manceau, A. (2008) Formation of Zn–Ca phyllomanganate nanoparticles in grass roots. *Geochimica et Cosmochimica Acta*, **72**, 2478–2490.

Lanson, B., Sakharov, B.A, Claret, F. and Drits, V.A. (2009) Diagenetic smectite-to-illite transition in clay-rich sediments: a reappraisal of X-ray diffraction results using the multi-specimen method. *American Journal of Science*, **309**, 476–516.

Lasaga, A.C. (1998) *Kinetic theory in the earth sciences.* Princeton University Press, Princeton, New Jersey, USA.

López-Arce, P., Gomez-Villalba, L.S., Pinho, L., Fernández-Valle, M.E., de Buergo, M.Á. and Fort, R. (2010) Influence of porosity and relative humidity on consolidation of dolostone with calcium hydroxide nanoparticles: Effectiveness assessment with non-destructive techniques. *Materials Characterization*, **61**, 168–184.

Manceau, A., Marcus, M.A., Grangeon, S., Lanson, M., Lanson, B., Gaillot, A.-C., Skanthakumar, S. and Soderholm, L. (2013) Short-range and long-range order of phyllomanganate nanoparticles determined using high-energy X-ray scattering. *Journal of Applied Crystallography*, **46**, 193–209.

Manzano, H., Dolado, J.S., Guerrero, A. and Ayuela, A. (2007) Mechanical properties of crystalline calcium-silicate-hydrates: comparison with cementitious C-S-H gels. *physica status solidi (a)*, **204**, 1775–1780.

Marty, N.C.M., Tournassat, C., Burnol, A., Giffaut, E. and Gaucher, E.C. (2009) Influence of reaction kinetics and mesh refinement on the numerical modelling of concrete/clay interactions. *Journal of Hydrology*, **364**, 58–72.

Marty, N.C.M., Cama, J., Sato, T., Chino, D., Villiéras, F., Razafitianamaharavo, A., Brendlé, J., Giffaut, E., Soler, J.M., Gaucher, E.C. and Tournassat, C. (2011)



https://doi.org/10.1180/minmag.2015.079.2.20 Published online by Cambridge University Press

Dissolution kinetics of synthetic Na-smectite. An integrated experimental approach. *Geochimica et Cosmochimica Acta*, **75**, 5849–5864.

McCulloch, C.E., Angus, M.J., Crawford, R.W., Rahman, A.A. and Glasser, F.P. (1985) Cements in radioactive waste disposal: some mineralogical considerations. *Mineralogical Magazine*, **49**, 211–221.

Merlet, C. (1994) An accurate computer correction program for quantitative electron probe microanalysis. *Mikrochimica Acta*, **114–115**, 363–376.

Merlino, S., Bonaccorsi, E. and Armbruster, T. (1999) Tobermorites; their real structure and order-disorder (OD) character. *American Mineralogist*, **84**, 1613–1621.

Merlino, S., Bonaccorsi, E. and Armbruster, T. (2001) The real structure of tobermorite 11Å: normal and anomalous forms, OD character and polytypic modifications. *European Journal of Mineralogy*, **13**, 577–590.

Metz, V. and Ganor, J. (2001) Stirring effect on kaolinite dissolution rate. *Geochimica et Cosmochimica Acta*, **65**, 3475–3490.

Morandeau, A., Thiéry, M. and Dangla, P. (2014) Investigation of the carbonation mechanism of CH and C-S-H in terms of kinetics, microstructure changes and moisture properties. *Cement and Concrete Research*, **56**, 153–170.

Nonat, A. (2004) The structure and stoichiometry of C-S-H. *Cement and Concrete Research*, **34**, 1521–1528.

Parkhurst, D.L. and Appelo, C.A.J. (1999) *User's Guide to PHREEQC (version 2): A computer program for speciation, batch-reaction, one-dimensional transport, and inverse geochemical calculations*. U.S. Department of the Interior, U.S. Geological Survey, Water-Resources Investigations Report **99-4259**.

Renaudin, G., Russias, J., Leroux, F., Cau-dit-Coumes, C. and Frizon, F. (2009) Structural characterization of C–S–H and C–A–S–H samples – Part II: Local environment investigated by spectroscopic analyses. *Journal of Solid State Chemistry*, **182**, 3320–3329.

Richardson, I.G. (2004) Tobermorite/jennite- and tobermorite/calcium hydroxide-based models for the structure of C-S-H: applicability to hardened pastes of tricalcium silicate, β-dicalcium silicate, Portland cement, and blends of Portland cement with blast-furnace slag, metakaolin, or silica fume. *Cement and Concrete Research*, **34**, 1733–1777.

Richardson, I.G. (2008) The calcium silicate hydrates. *Cement and Concrete Research*, **38**, 137–158.

Šauman, Z. (1971) Carbonization of porous concrete and its main binding components. *Cement and Concrete Research*, **1**, 645–662.

Savage, D. (2011) A review of analogues of alkaline alteration with regard to long-term barrier performance. *Mineralogical Magazine*, **75**, 2401–2418.

Schneider, J., Cincotto, M.A. and Panepucci, H. (2001) $^{29}$Si and $^{27}$Al high-resolution NMR characterization of calcium silicate hydrate phases in activated blast-furnace slag pastes. *Cement and Concrete Research*, **31**, 993–1001.

Schweizer, C.R. (1999) *Calciumsilikathydrat-Mineralien: Lösungskinetik und ihr Einfluss auf das Auswaschverhalten von Substanzen aus einer Ablagerung mit Rückständen aus Müllverbrennungsanlagen*. PhD thesis, University of Basel, Switzerland, p. 113.

Skinner, L.B., Chae, S.R., Benmore, C.J., Wenk, H.R. and Monteiro, P.J.M. (2010) Nanostructure of calcium silicate hydrates in cements. *Physical Review Letters*, **104**, 195502.

Sugiyama, D. (2008) Chemical alteration of calcium silicate hydrate (C–S–H) in sodium chloride solution. *Cement and Concrete Research*, **38**, 1270–1275.

Suzuki, K. and Nishikawa, T. and Ito, S. (1985) Formation and carbonation of C-S-H in water. *Cement and Concrete Research*, **15**, 213–224.

Taylor, H.F.W. (1986) Proposed structure for calcium silicate hydrate gel. *Journal of the American Ceramic Society*, **69**, 464–467.

Trapote-Barreira, A., Cama, J. and Soler, J.M. (2014) Dissolution kinetics of C–S–H gel. Flow-through experiments. *Physics and Chemistry of the Earth, Parts A/B/C*, **70–71**, 17–31.

Vandamme, M. and Ulm, F.J. (2013) Nanoindentation investigation of creep properties of calcium silicate hydrates. *Cement and Concrete Research*, **52**, 38–52.

Vieillard, P. and Rassineux, F. (1992) Thermodynamic and geochemical modelling of the alteration of two cement matrices. *Applied Geochemistry*, **7, Supplement 1**, 125–136.

Villain, G., Thiery, M. and Platret, G. (2007) Measurement methods of carbonation profiles in concrete: Thermogravimetry, chemical analysis and gammadensimetry. *Cement and Concrete Research*, **37**, 1182–1192.

Watson, C.E., Savage, D., Wilson, J., Walker, C. and Benbow, S.J. (2012) The long-term cement studies project: the UK contribution to model development and testing. *Mineralogical Magazine*, **76**, 3445–3455.

Wilson, J.C., Benbow, S.J., Metcalfe, R., Savage, D., Walker, C.S. and Chittenden, N. (2011) Fully coupled modeling of long term cement well seal stability in the presence of $CO_2$. *Energy Procedia*, **4**, 5162–5169.



https://doi.org/10.1180/minmag.2015.079.2.20 Published online by Cambridge University Press